



# Ga-substituted $\text{Li}_7\text{La}_3\text{Zr}_2\text{O}_{12}$ : An investigation based on grain coarsening in garnet-type lithium ion conductors



Changlong Li <sup>a</sup>, Yufei Liu <sup>b</sup>, Jian He <sup>b</sup>, Kyle S. Brinkman <sup>a,\*</sup>

<sup>a</sup> Department of Materials Science and Engineering, Clemson University, Clemson, SC 29634, USA

<sup>b</sup> Department of Physics and Astronomy, Clemson University, Clemson, SC 29634, USA

## ARTICLE INFO

### Article history:

Received 16 September 2016

Received in revised form

14 October 2016

Accepted 19 November 2016

Available online 2 December 2016

### Keywords:

Gallium doping

Lithium ion conduction

Spark plasma sintering

Solid state electrolytes

## ABSTRACT

Gallium substituted garnet-type  $\text{Li}_7\text{La}_3\text{Zr}_2\text{O}_{12}$  has been synthesized via a sol-gel (SG) and solid-state reaction (SSR) routes. The results of scanning electron microscopy measurements showed that the SG process produced statistically smaller powder particles than the SSR route. A structural transformation from tetragonal to cubic phase occurs at an elevated level of Gallium doping, resulting in a cubic structure for  $\text{Li}_{5.5}\text{La}_3\text{Zr}_2\text{Ga}_{0.5}\text{O}_{12}$  (0.5Ga-LLZO). To facilitate the comparison of sintering procedures, powders of Ga-doped LLZO were sintered by both a conventional sintering process and a spark plasma sintering (SPS) process. For pellets sintered by SPS at 950 °C for 5 min, grain coarsening was limited due to the short sintering duration. However, grain coarsening was observed in the SPS pellets sintered at 950 °C, 1000 °C, and 1100 °C for 5 h in air. The ionic conductivity was determined by electrochemical impedance spectroscopy (EIS) at temperatures in the range of 20 °C–100 °C. The total ionic conductivity was found to increase with increased relative density and larger grain size. The highest total ionic conductivity at room temperature was found to be in the range of  $5.81 \times 10^{-5}$  S/cm ( $E_a = 0.41$  eV) in this work.

© 2016 Elsevier B.V. All rights reserved.

## 1. Introduction

There is an increasing demand for high energy density, long recycling life and safer batteries for portable electric devices and electric vehicles, and rechargeable lithium ion batteries have attracted significant attention. However, the state-of-the-art electrolytes used in lithium ion batteries still employ an organic Li-ion salt electrolyte that has posed safety concerns arising from dendrite formation and flammability [1]. In addition, the stability problem of the aqueous electrolytes with lithium metal has seriously limited the voltage range [2,3]. To address these concerns, solid-state electrolytes with enhanced safety and room temperature conductivities in excess of  $10^{-4}$  S/cm are being considered as a substitute for current liquid electrolytes and polymer-based separators. The employment of anode materials like  $\text{LiC}_6$ , lithium metals, and Nickel-, Cobalt-, Iron- or Manganese-containing oxides like  $\text{LiNi}_{1/3}$

$\text{Mn}_{1/3}\text{Co}_{1/3}\text{O}_4$  as cathode materials results in much higher energy and powder densities as well as higher long-term stability [3].

A group of garnet-type fast lithium ionic conductors with the chemical formula of  $\text{Li}_5\text{La}_3\text{M}_2\text{O}_{12}$  ( $M = \text{Nb}, \text{Ta}$ ) was reported by Weppener et al. in 2003.  $\text{Li}_5\text{La}_3\text{Nb}_2\text{O}_{12}$  and  $\text{Li}_5\text{La}_3\text{Ta}_2\text{O}_{12}$  exhibited the same magnitude of bulk ionic conductivity  $\sim 10^{-6}$  S/cm at 25 °C [4].  $\text{Li}_6\text{BaLa}_2\text{Ta}_2\text{O}_{12}$  possessed a higher conductivity of  $4 \times 10^{-5}$  S/cm at 22 °C with an activation energy of 0.40 eV [5]. Zirconium-containing garnet lithium has been investigated based on the good thermal and chemical stability against metallic lithium, as well as the low cost and ease of preparation. In terms of structure, a higher packing density is essential to provide enough pathways for lithium ions transport between adjacent lattice sites. Therefore, a high sintering temperature and longer sintering duration are essential to obtain dense electrolytes. Murugan et al. have firstly reported  $\text{Li}_7\text{La}_3\text{Zr}_2\text{O}_{12}$  (LLZO) with high bulk lithium ionic conductivity of approximately  $10^{-4}$  S/cm at 25 °C via SSR procedure at 1230 °C for 36 h [6]. However, lithium loss leading to the formation of a pyrochlore phase  $\text{La}_2\text{Zr}_2\text{O}_7$  typically appears at 1250 °C [7,8].

Two distinct crystalline phases (cubic and tetragonal) of LLZO in different temperature range were identified by Awaka et al. [2,9]

\* Corresponding author.

E-mail address: [ksbrink@clemson.edu](mailto:ksbrink@clemson.edu) (K.S. Brinkman).

with only cubic structured LLZO exhibiting high lithium ion conductivity [9]. In general, lithium ion conductivity of the cubic phase LLZO is higher than that of tetragonal LLZO by two orders of magnitude. However, the mechanism of the phase transformation between these two phases is not completely understood. Multiple doping strategies have been tried by previous researchers to stabilize the cubic structure of LLZO at room temperature such as Aluminum(Al) [10–14], Yttrium(Y) [15], Gallium(Ga) [11,16,17], Tantalum(Ta) [11,18], Niobium(Nb) [19], Tungsten(W) [20].

In this work, the grain size of  $\text{Li}_{5.5}\text{Ga}_{0.5}\text{La}_3\text{Zr}_2\text{O}_{12}$  (0.5Ga-LLZO) has been controlled by a spark plasma sintering (SPS) method. Grain coarsening was achieved when the SPS pellets were subsequently sintered in a conventional box furnace with increased temperature and time. Similar treatment have been done in our previous work on proton conducting ceramics to gain insight into the role of grain boundaries on ionic conductivity [21]. Compared with conventional sintering techniques such as hot press, spark plasma sintering (SPS) facilitates a pulse current driven through the sample as well as the surrounded graphite die. SPS has been found to be a quick and effective method for densification. Unlike hot press where the sample is heated by the heating element, in the SPS process, the pulse current enhances the interaction between adjacent grains, which facilitates densification.

## 2. Experimental

### 2.1. Synthesis of LLZO and Ga-doped LLZO via a solid-state route

Raw powders of  $\text{Li}_2\text{CO}_3$  (99.9%, Macron Fine Chemicals<sup>®</sup>),  $\text{La}_2\text{O}_3$  (99.99%, Alfa Aesar<sup>®</sup>) and  $\text{ZrO}_2$  (99.7%, Alfa Aesar<sup>®</sup>) were mixed with the corresponding molar ratio, as well as  $\text{Ga}_2\text{O}_3$  (99%, Alfa Aesar<sup>®</sup>) to form the targeted composition ( $\text{Li}_{7-3x}\text{Ga}_x\text{La}_3\text{Zr}_2\text{O}_{12}$ ,  $x = 0, 0.1, 0.5, 1.0$ ). The mixture was then ball-milled with zirconia balls for 48 h with ethanol as the dispersing reagent. 10% excess of lithium carbonate was added in order to compensate for the loss of lithium at later high heating stage. The mixture was moved into a baker with a mesh filter and then dried in the oven at 100 °C for 12 h. The dried powders were then pressed into pellets under isostatic pressure and heated at 950 °C for 5 h in air. The annealed pellets were ground again and re-compressed into pellets. Calcination was repeated at 950 °C two times to ensure the complete reaction of starting materials.

### 2.2. Synthesis of LLZO and 0.5Ga-LLZO raw powder via a SG route

The precursor of LLZO via the SG route was made from the starting materials  $\text{Li}_2\text{CO}_3$  (99%, Alfa Aesar<sup>®</sup>),  $\text{La}(\text{NO}_3)_3 \cdot 6\text{H}_2\text{O}$  (99%, Alfa Aesar<sup>®</sup>) and  $\text{ZrO}(\text{NO}_3)_2 \cdot x\text{H}_2\text{O}$  (99%, Sigma-Aldrich<sup>®</sup>) in the stoichiometric proportions. First, citric acid was dissolved in water as the complexing reagent.  $\text{ZrO}(\text{NO}_3)_2 \cdot x\text{H}_2\text{O}$  was then dissolved in the distilled water and nitric acid, in which nitric acid dissolved  $\text{ZrO}(\text{NO}_3)_2 \cdot x\text{H}_2\text{O}$ , and  $\text{GaCl}_3$  (99.99%, Sigma Aldrich<sup>®</sup>).  $\text{LiNO}_3$  and  $\text{La}(\text{NO}_3)_3 \cdot 6\text{H}_2\text{O}$  powders were dissolved in the mixture of  $\text{Zr}^{4+}$  and citric acid solution, pre-treated  $\text{GaCl}_3$  solution were then added to form the targeted composition 0.5Ga-LLZO ( $\text{Li}_{5.5}\text{Ga}_{0.5}\text{La}_3\text{Zr}_2\text{O}_{12}$ ). The transparent solution was stirred at room temperature overnight and then heated to a gel at 100 °C for several days with multiple grinding steps until all the gel became powder (dried precursor). The dried precursor of LLZO was heated in the box furnace at 950 °C for 5 h. This calcination step was repeated two times, similar to the heat treatment used in the solid-state synthesis process. Following calcination, the powders were ground into very fine powder particles and combined with 5 wt% polyvinyl alcohol (PVA) as a ceramic binder. The powders were fabricated into pressed pellets with an isostatic press operating at 1400 psi for 1 min.

### 2.3. Conventional sintering vs. spark plasma sintering

Sintering was performed in air in a box furnace with the samples resting on an alumina plate with a covered alumina crucible. The crucible and plate were sealed using a ceramic paste in order to avoid excessive lithium loss during the sintering process. In addition, experiments were conducted with platinum foil between the pellets and the alumina crucible to limit incorporation of Al into the samples. Pellets were sintered at various temperatures from 950 °C to 1200 °C with a heating/cooling rate of 5 °C/min. A small boat of  $\text{Li}_2\text{CO}_3$  was put next to the pellets producing a lithium rich vapor phase intended to further reduce lithium loss from the pellets during the sintering process, similar work has been done in the previous work [22].

The mixed powder synthesized via SG process was loaded in a graphite die/punches set with an inner diameter of 12.7 mm. Two pieces of graphite foils were used as spacers to separate the powder and graphite punches. The sample was then placed in the SPS chamber and heated up to the target temperature. Several different SPS conditions were tried and tested: samples were applied with a pressure of 3kN/6kN, sintering temperature of 800 °C, 900 °C, and 950 °C, and sintering duration of 5 min and 10 min. It was found that the pellet sintered at 950 °C for 5 min and with 6kN pressure is the most solid, with a density of 4.18 g/cm<sup>3</sup>. On the other hand, all the pellets sintered with the sintering duration of 10 min cracked.

## 3. Results and discussion

### 3.1. Phase analysis and morphology

The synthesized powders and sintered pellets were analyzed by X-ray diffraction (XRD) using  $\text{CuK}\alpha$  radiation at room temperature in the  $2\theta$  ranges from 10° to 70° with 1°/min scanning rate. For undoped LLZO powders, the XRD patterns exhibited peaks matching the tetragonal structure, which was consistent with the literature [23,24]. The main impurity typically observed in LLZO is the pyrochlore phase  $\text{La}_2\text{Zr}_2\text{O}_7$  [6,23–36]. Pyrochlore is also the dominant impurity phase in similar compositions such as perovskite type  $\text{La}_{0.5}\text{Li}_{0.5}\text{TiO}_3$  [37]. This secondary phase is commonly observed after pellets are sintered due to the loss of lithium at high temperatures. Other impurities such as  $\text{Li}_2\text{ZrO}_3$  have also been observed and reported in the recent literature [38–40]. In Fig. 1, a structural transformation from tetragonal symmetry to cubic symmetry was observed in the present work with increasing

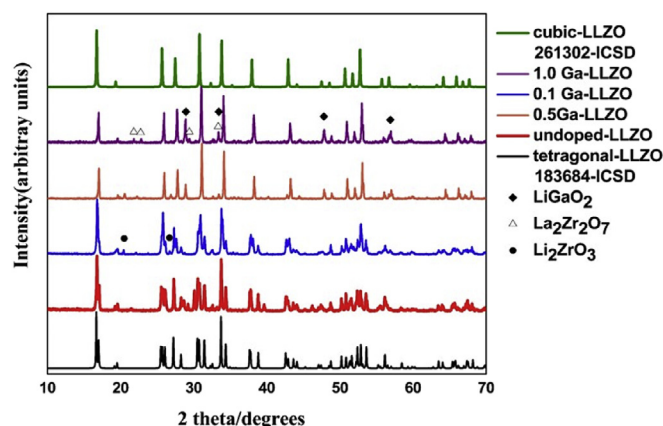


Fig. 1. X-ray diffraction patterns for LLZO, 0.1Ga-LLZO, 0.5Ga-LLZO, 1.0Ga-LLZO powders synthesized via SSR process, and the standard patterns for tetragonal-LLZO (ICSD\_183684) [41], standard cubic-LLZO (ICSD\_261302) [42]. Secondary phase  $\text{La}_2\text{Zr}_2\text{O}_7$  (PDF 71-2363);  $\text{Li}_2\text{ZrO}_3$  (PDF 75-2157);  $\text{LiGaO}_2$  (PDF 72-1640).

**Table 1**  
SSR powders phase structure types and lattice parameters.

Nomination	Composition	Structure type	Lattice parameters
LLZO	$\text{Li}_7\text{La}_3\text{Zr}_2\text{O}_{12}$	Tetragonal	$a = b = 13.114(0)$ $c = 12.690(7)$
0.1Ga-LLZO	$\text{Li}_{6.7}\text{Ga}_{0.1}\text{La}_3\text{Zr}_2\text{O}_{12}$	Tetragonal and cubic	
0.5Ga-LLZO	$\text{Li}_{5.5}\text{Ga}_{0.5}\text{La}_3\text{Zr}_2\text{O}_{12}$	Cubic	$c = 12.980(4)$
1.0Ga-LLZO	$\text{Li}_4\text{GaLa}_3\text{Zr}_2\text{O}_{12}$	Cubic	$c = 13.015(7)$

amount of gallium substitution. XRD investigations indicate that 0.1Ga-LLZO is a mixture of tetragonal phase and cubic phases, however the composition 0.5Ga-LLZO is primarily a cubic phase with small amounts of impurities such as  $\text{LiZrO}_3$ , which are commonly observed in literature. The structure type and lattice parameters are summarized in Table 1. The composition 1.0Ga-LLZO revealed excess Ga in the form of  $\text{LiGaO}_2$  according to XRD measurements and SEM-EDS elemental mapping. Therefore the focus of this work was on the comparison of un-doped LLZO and 0.5Ga-LLZO via SG route as displayed in Fig. 2 with the lattice parameters summarized in Table 2.

### 3.2. Powder particle size analysis: SG versus SSR route

LLZO powders synthesized via a SG and a SSR process were dispersed in ethanol after ultrasonic treatment. The powders were deposited on a silicon plate and dried in the oven at 80 °C for 24 h. Powders derived from a SG (Fig. 3a) and SSR (Fig. 3c) were detected by scanning electron micro-spectroscopy (SEM) after coating with platinum. Distribution of powder particle sizes have been statistically analyzed by the ImageJ<sup>®</sup> software [43]. The mean size of powder particles synthesized by the SG method 0.73  $\mu\text{m}$  with a standard deviation  $\sim 0.22 \mu\text{m}$  as indicated in Fig. 3b. The SSR process produced particles in the mean size range of 2.47  $\mu\text{m}$  with a standard deviation  $\sim 0.70 \mu\text{m}$  as shown in Fig. 3d. The results indicate that particles synthesized via the SG are much smaller than those obtained from SSR route. This smaller size would affect the sintering process regarding elemental distribution and grain coarsening.

### 3.3. A smaller powder particle size is beneficial to grain coarsening during sintering stage

0.5Ga-LLZO was chosen as the targeted composition to be compared between the SG process and the SSR process due to the single cubic phase observed in the calcined powders. The sample

**Table 2**  
SG powders phase structure types and lattice parameters comparison.

Nomination	Composition	Structure type	Lattice parameters
LLZO	$\text{Li}_7\text{La}_3\text{Zr}_2\text{O}_{12}$	Tetragonal	$a = b = 13.132(1)$ $c = 12.679(4)$
0.5Ga-LLZO	$\text{Li}_{5.5}\text{Ga}_{0.5}\text{La}_3\text{Zr}_2\text{O}_{12}$	Cubic	$a = b = c = 12.980(6)$

nomenclature and fabrication processes for these experiments are summarized in Table 3. 0.5Ga-LLZO synthesized by SSR and sintered by conventional sintering at 1000 °C for 5 h is displayed in Fig. 4(a) and 1100 °C is displayed in Fig. 4b. Spherical grains were observed in the range of  $\sim 5 \mu\text{m}$ , with peripheral connections forming fringes. Compared with the pellets sintered at 1000 °C by conventional sintering, pellets sintered at the same temperature exhibited larger grains with obvious grain boundaries. Fig. 4c and (d) show the pellets synthesized by the SG process have higher sinterability than those synthesized by SSR. The grains size is in the ranges of  $\sim 100 \mu\text{m}$ , which is about 20 times larger than those synthesized by SSRs. Densification of the pellets and good inter-grain connectivity are clearly visible in the SEM images, further indicating that finer powder particles in the SG synthesis process are more favorable for sintering. A uniform distribution of elements in the bulk of the material is exhibited for the 0.5Ga-LLZO sample according to SEM-EDS analysis in Fig. 5. An increased concentration of Ga was observed at the grain boundaries.

### 3.4. Grain coarsening in 0.5Ga-LLZO SPS pellets

Pellets of 0.5Ga-LLZO fabricated from the SG powders have been sintered by spark plasma sintering method at 950 °C for 5 min. The grain size was controlled and limited with reduced sintering duration. Previous studies on the powders synthesized via both SG route and by SSR method showed the SG powders resulted in finer particle size, compared with SSR powders. In general, finer powder particles are more beneficial for sintering resulting in lower sintering temperature and enhanced grain growth. The sintering temperature for the powders synthesized via SG process is much lower than those synthesized via SSR process due to the higher energy activity of the smaller powder particles. Meantime, these finer powder particles also promote grain coarsening with prolonged sintering duration. The sample nomenclature and fabrication process for this series of samples is summarized in Table 4.

Obviously, a large ratio of grain/grain-boundaries can be realized by increasing the grain size. Compared with pellets fabricated from the SSR powders, the pellets fabricated by SG powders possessed larger grains. Investigations on the impact of grain coarsening on conductivity initiated with the pellets fabricated with SG powders and sintered by the spark plasma sintering (SPS) method for 5 min. After the initial SPS treatment, the pellets were subjected to conventional sintering at 950 °C, 1000 °C, 1100 °C for 5 h consequently. SEM images of the surface of these pellets are shown in Fig. 6. The powder particles size distributions were analyzed by ImageJ<sup>®</sup> software [43] and the plots of particle size distribution are presented in Fig. 7, particle size did exhibit significant change due to the elevated sintering temperatures were employed. The average grain size changed from 1.34  $\mu\text{m}$  to 3.51  $\mu\text{m}$ , and then from 7.03  $\mu\text{m}$  after the heat-treatment at 950 °C, 1000 °C and 1100 °C respectively. Grain and grain size distribution analysis of 0.5Ga-LLZO\_CS1100\_5 h shows the mean grain size in the pellets is 102.40  $\mu\text{m}$  in Section 3.3.

### 3.5. Lithium ionic conductivity (0.5Ga-LLZO)

Lithium ionic conductivities of 0.5Ga-LLZO pellets were determined by Electrochemical Impedance Spectroscopy (Solartron<sup>®</sup>, SI

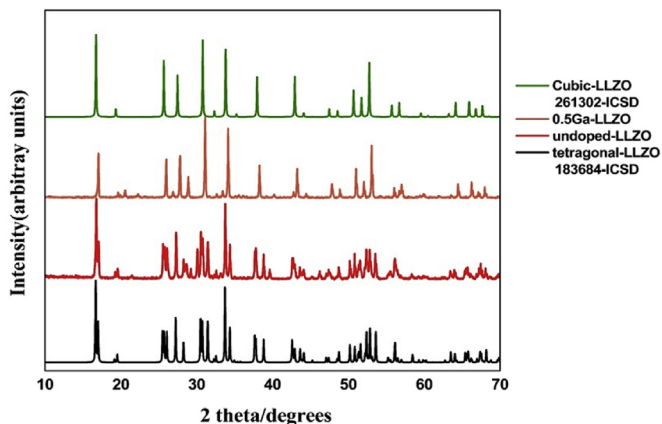


**Fig. 2.** X-ray diffraction patterns for LLZO and 0.5Ga-LLZO powders synthesized via SG process, and the standard patterns for tetragonal-LLZO(ICSD\_183684) [41], standard cubic-LLZO(ICSD\_261302) [42], Secondary phase  $\text{La}_2\text{Zr}_2\text{O}_7$ (PDF 71-2363);  $\text{Li}_2\text{ZrO}_3$ (PDF 75-2157);  $\text{LiGaO}_2$ (PDF 72-1640).

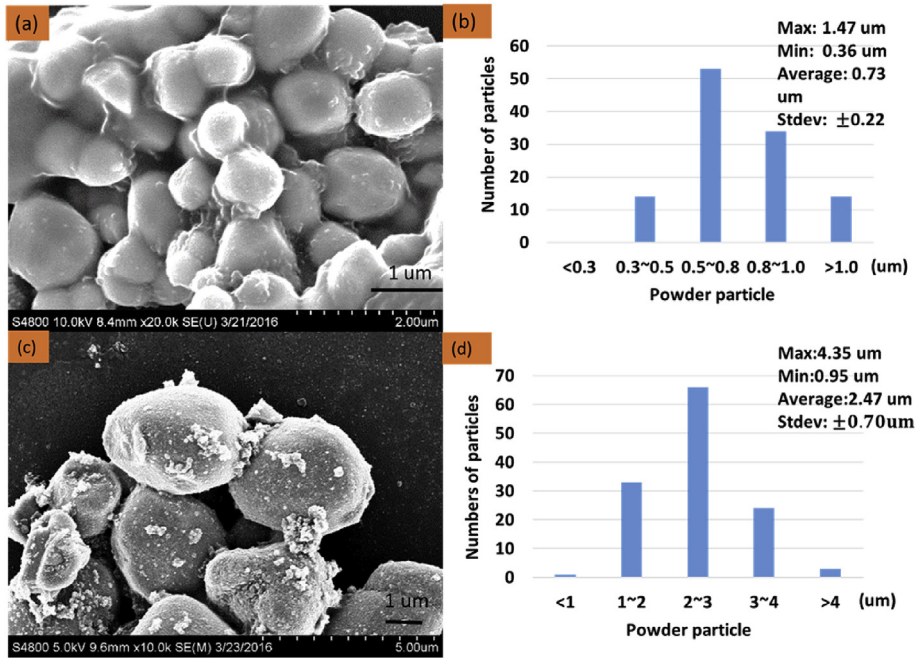


**Fig. 3.** (a) Scanning electron microscopy (SEM) images of LLZO powders synthesized via SG process; (b) Powder particle size distribution of powders synthesized via SG process; (c) Scanning electron microscopy (SEM) images of LLZO powders synthesized via SSR process; (d) Powder particle size distribution of powders synthesized via SSR process.

**Table 3**  
0.5Ga-LLZO Sample nomenclature and fabrication process. Nomination Fabrication process.

Pellets Name	Fabrication process
SPS950_5 min	Pellets sintered by SPS at 950 °C for 5 min
SPS + CS950_5 h	The SPS950_5 min pellets continually sintered by conventional sintering method in box furnace at 950 °C for 5 h
SPS + CS1000_5 h	The SPS + CS950_5 h pellets continually sintered by conventional sintering method in box furnace at 1000 °C for 5 h
SPS + CS1100_5 h	The SPS + CS1100_5 h pellets continually sintered by conventional sintering method in box furnace at 1100 °C for 5 h

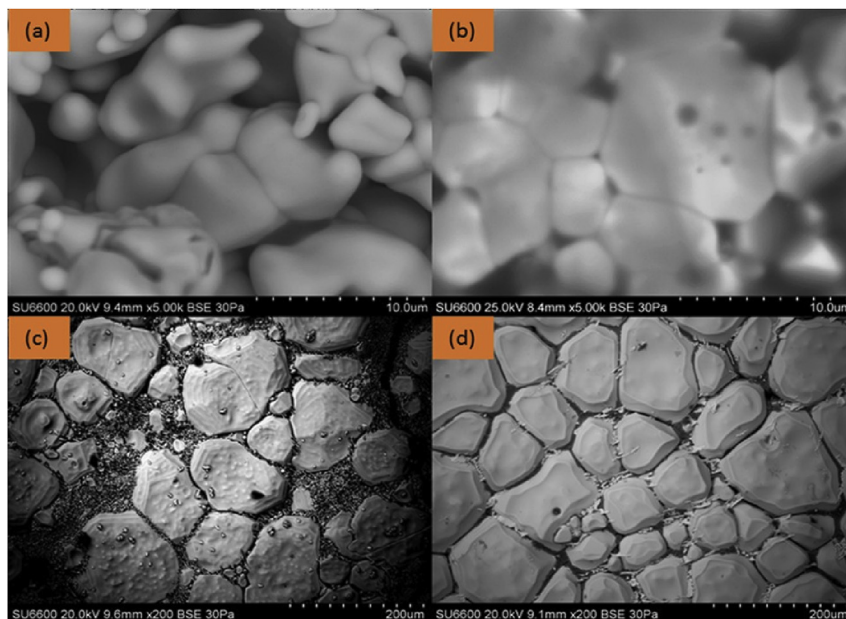


**Fig. 4.** Scanning electron microscopy (SEM) images of (a) 0.5Ga-LLZO\_SSR\_CS1000, magnitude 5 K (b) 0.5Ga-LLZO\_SSR\_CS1100, magnitude 5 K (c) 0.5Ga-LLZO\_SG\_CS1000, magnitude 5 K (d) 0.5Ga-LLZO\_SG\_CS1100, magnitude 5 K.

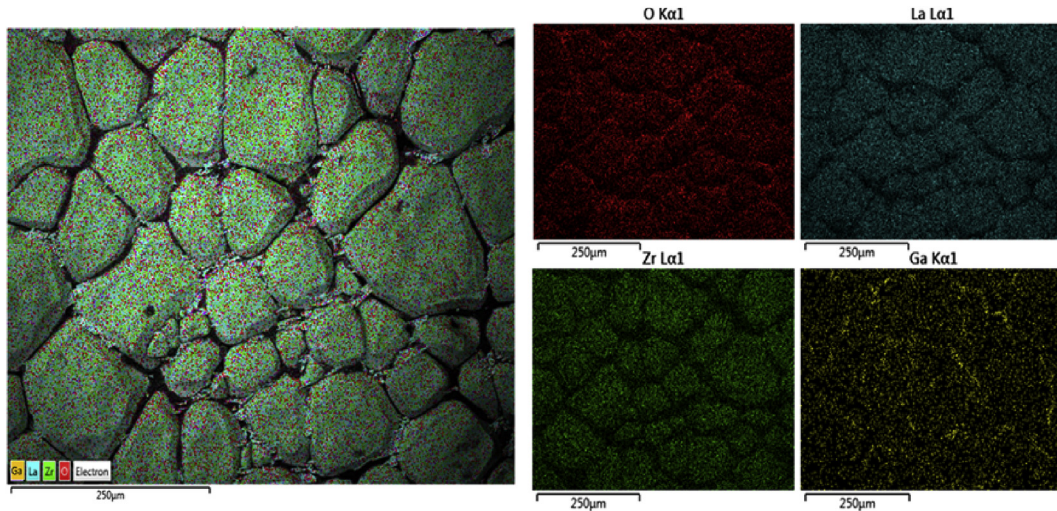


Fig. 5. SEM-EDS image of pellet 0.5Ga-LLZO\_SG\_CS1100 indicates O, La, Zr, Ga distribute homogeneously and Ga rich phases concentrate on the grain boundaries.

**Table 4**  
0.5Ga-LLZO Sample nomenclature and fabrication process.

Nomination	Fabrication process
0.5Ga-LLZO_SSR_CS1000	Li <sub>5.5</sub> Ga <sub>0.5</sub> La <sub>3</sub> Zr <sub>2</sub> O <sub>12</sub> pellets fabricated from SSR route and sintered by conventional sintering process at 1000 °C for 5 h in air
0.5Ga-LLZO_SSR_CS1100	Li <sub>5.5</sub> Ga <sub>0.5</sub> La <sub>3</sub> Zr <sub>2</sub> O <sub>12</sub> pellets fabricated from SSR route and sintered by conventional sintering process at 1100 °C for 5 h in air
0.5Ga-LLZO_SG_CS1000	Li <sub>5.5</sub> Ga <sub>0.5</sub> La <sub>3</sub> Zr <sub>2</sub> O <sub>12</sub> pellets fabricated from SG route and sintered by conventional sintering process at 1000 °C for 5 h in air
0.5Ga-LLZO_SG_CS1100	Li <sub>5.5</sub> Ga <sub>0.5</sub> La <sub>3</sub> Zr <sub>2</sub> O <sub>12</sub> pellets fabricated from SG route and sintered by conventional sintering process at 1000 °C for 5 h in air
Nomination	Fabrication process

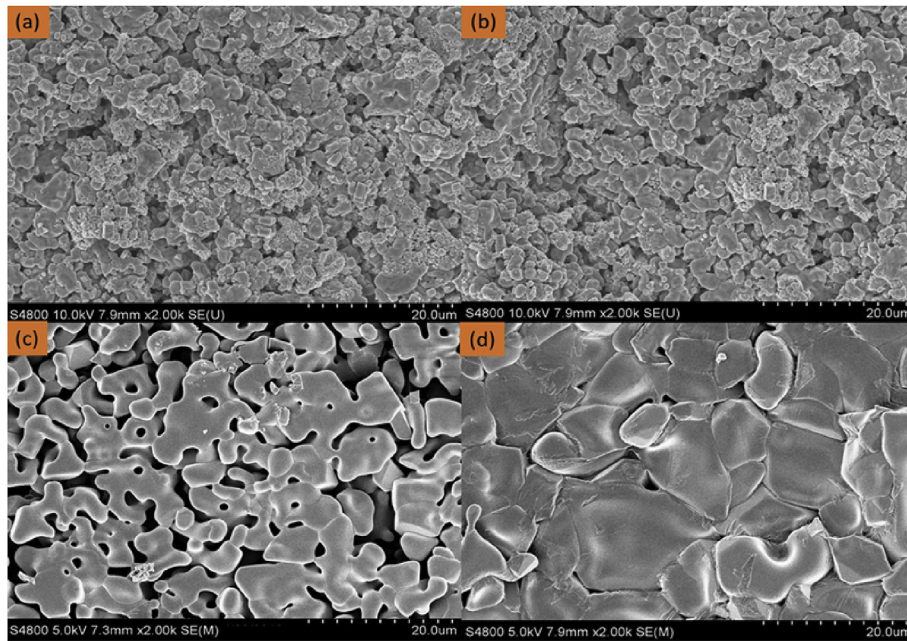


Fig. 6. Scanning electron microscopy (SEM) images of 0.5Ga-LLZO\_SG sintered by (a) SPS950\_5 min, 2 K, (b) SPS + CS950\_5 h, 2 K, (c) SPS + CS1000\_5 h, 2 K (d) SPS + CS1100\_5 h, 2 K. SG means the powders synthesized via sol-gel route, CS950\_5 h, CS1000\_5 h, and CS1100\_5 h represents the SPS950 with reheating treatment at 950 °C, 1000 °C and 1000 °C for 5 h.

1287 + SI 1260) with pasted Ag on both sides of the pellets as the electrodes. EIS was tested in air in a tube furnace in the temperature range from room temperature (RT) to 100 °C. According to relations between conductivity and impedance,  $R = 1/\sigma \times L/A$ , conductivities can be obtained by the calculation of impedance and the dimension of the pellets. In the equation, R is the impedance obtained in EIS

measurement; L is the thickness of the pellets; A is the surface area of the pellets; and  $\sigma$  is the conductivity.

The Nyquist plots of the 0.5Ga-LLZO pellets measured at room temperature are shown in Fig. 8. The equivalent circuits of  $R_b(R_{gb}Q_{gb})$  have been employed here to fit the experimental data. In which,  $R_b$  donates the bulk resistance,  $R_{gb}$  donates the grain-grain

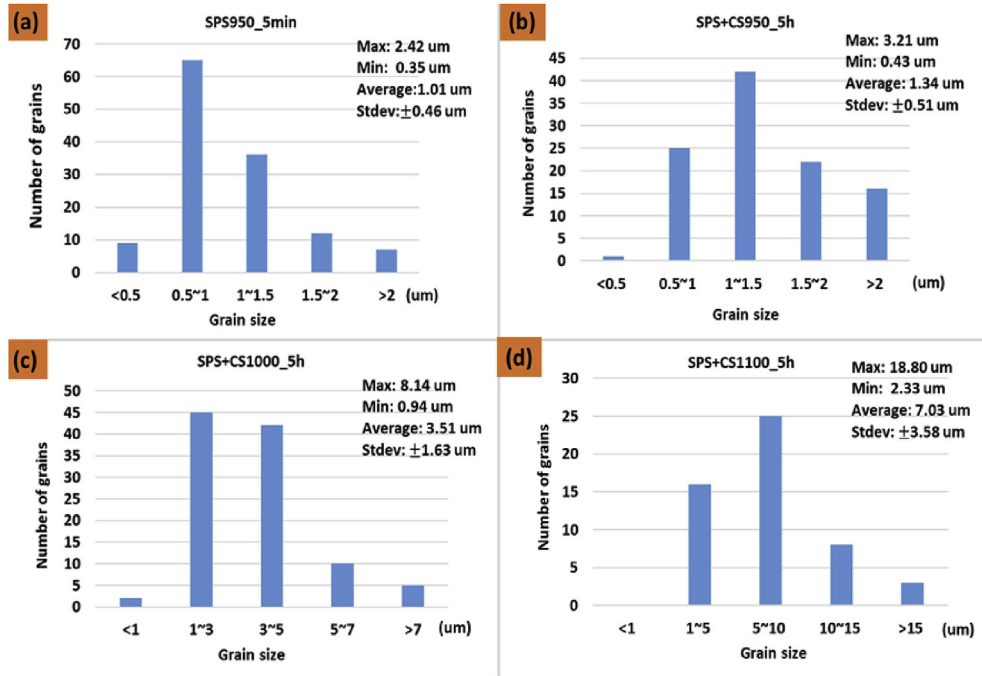


Fig. 7. Grain size distribution plots of 0.5Ga-LLZO pellets sintered by (a) SPS950\_5 min (b)SPS + CS950\_5 h (c) SPS + CS1000\_5 h (d) SPS + CS1000\_5 h.

boundary resistance, and  $Q_{gb}$  the constant phase element contributions of the grain-grain boundary.

In the pellets, both bulk and grain-boundary regions have contributions to the total conductivity. In the view of impedance,  $R_t = R_b + R_{gb}$ .  $R_b$  and  $R_{gb}$  can be obtained via the equivalent circuit and Z-view software<sup>®</sup>. Thereby,  $\sigma_b$ ,  $\sigma_{gb}$ , and  $\sigma_t$  was finally obtained via  $R_b R_{gb} R_t$ , correspondingly.

From the microstructural perspective, there was no obvious change from SPS950\_5 min to SPS + CS950\_5 h. However, electrical measurements indicate that the bulk conductivity ( $\sigma_b$ ) became larger and grain boundaries conductivity ( $\sigma_{gb}$ ) became smaller after prolonged annealing at 950 °C. For 1000 °C, 1100 °C, both the bulk ( $\sigma_b$ ) and grain-boundary ( $\sigma_{gb}$ ) ionic conductivity have been improved as a result of the enhanced grain growth. The larger grain sizes lead to an enhancement in the ratio of grain/grain boundaries, resulting the improvement in the total ionic conductivities.

The sample SPS + CS1100\_5 h, which was made from SG powders and sintered by the conventional sintering process resulted in the highest ionic conductivity bulk and grain-boundary conductivity measured in this study. That is perhaps due to the different level of grain coarsening from the initial state. Compared with the SPS + CS1100\_5 h pellet (mean grain size~7.03  $\mu\text{m}$ ), the CS1100\_5 h exhibited much larger grains (mean grain size~104.20  $\mu\text{m}$ ), resulting in enhanced conductivity.

The temperature dependent total ionic conductivities for 0.5Ga-LLZO sintered by SPS and continually sintered by conventional sintering was plotted according to the Arrhenius equation

$$\sigma_T = \sigma_0 \exp(-E_a/kT)$$

where  $\sigma_0$  is a pre-exponential factor proportional to the number of carrier ions;  $E_a$  is the activation energy in eV, k is the Boltzmann

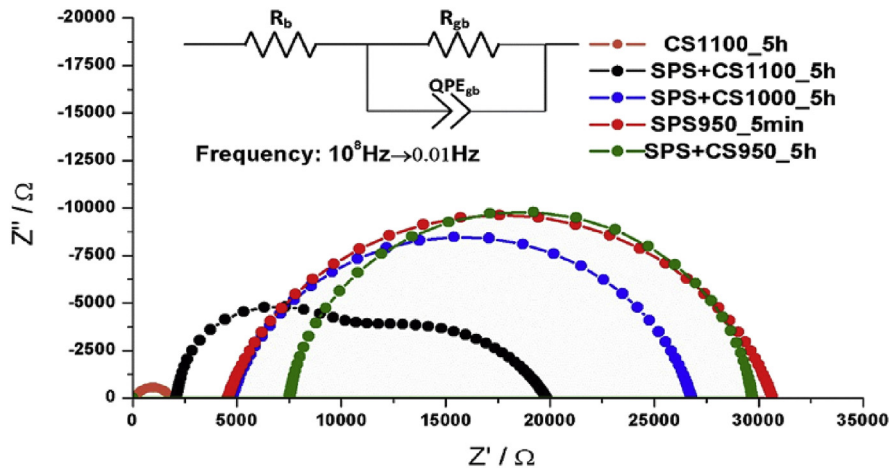
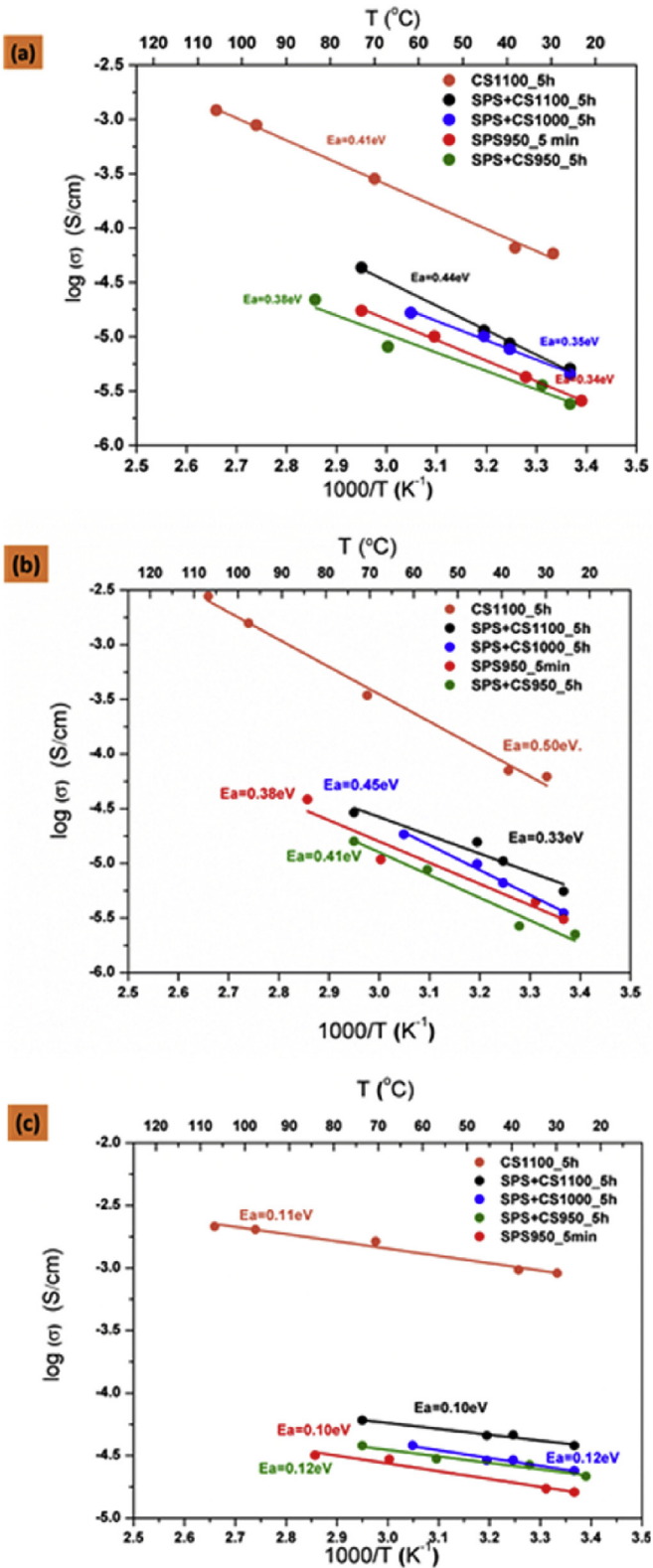


Fig. 8. Nyquist plots of 0.5Ga-LLZO\_SPS950 pellets prepared by spark plasma sintering (SPS) for 5 min, SPS + CS950\_5 h (Conventional sintering at 950 °C for 5 h), SPS + CS1000\_5 h (Conventional sintering at 1000 °C for 5 h), SPS + CS1100\_5 h (Conventional sintering at 1100 °C for 5 h) and 0.5Ga-LLZO\_CS1100 (Conventional sintering at 1100 °C for 5 h directly from calcined powders) measured at room temperature (RT). All the powders were synthesized via SG process.



**Fig. 9.** Arrhenius plots of (a) total ionic conductivities, (b) grain-boundary ionic conductivity and (c) bulk ionic conductivity of 0.5Ga-LLZO\_SPS950 pellets: SPS950\_5 min (sintered by SPS for 5 min), SPS + CS950\_5 h (conventional sintering at 950 °C for 5 h), SPS + CS1000\_5 h (conventional sintering at 1000 °C for 5 h), SPS + CS1100\_5 h (conventional sintering at 1100 °C for 5 h) and 0.5Ga-LLZO\_CS1100 (conventional sintering at 1100 °C for 5 h directly from calcined powders) measured in the temperature range 20–100 °C.

constant of  $8.62 \times 10^{-5}$  eV/K; and  $T$  is the absolute temperature in K. The activation energy was obtained by fitting the Arrhenius plot and calculated by the slope of the fitted line are displayed in Fig. 9 for (a) total ionic conductivities, (b) grain-boundary ionic conductivity and (c) bulk ionic conductivity. Values of activation energy for bulk region are very closed to each other, which indicate the mechanism of ion transport in the material are similar. The difference in activation energy at the grain-boundary and total ionic conductivity indicate the mechanisms of transport at the interface could be different. It is known that grain boundary structure is disordered and the crossover from periodic bulk structure to disordered interface could disrupt ion motion ([44]). Possible impacts such as grain size and density should be taken into consideration for these varieties in activation energy.

In general, there will be an optimum trade-off between lithium-loss, sintering temperature, phase composition and the ionic conductivity of the pellets. The highest total ionic conductivity at room temperature was found to be in the range of  $5.81 \times 10^{-5}$  S/cm ( $E_a = 0.41$  eV) for the SG synthesized 0.5Ga-LLZO and sintered by conventional sintering in the air. The total conductivity is comprised of bulk (grain) and grain boundaries (interface) contributions. Generally speaking, the bulk region displayed one to two order higher magnitude increase as compared to the grain-boundary ionic conductivity. This points to a metric of the ratio of grain/grain-boundaries area, which could be used for optimization

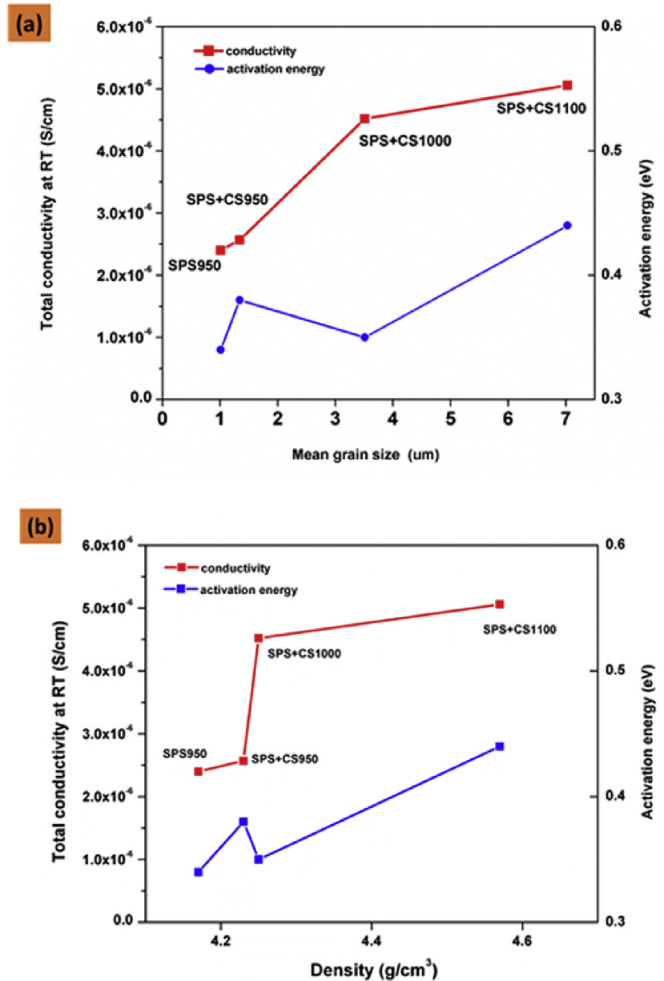


**Fig. 10.** The relationship between ionic conductivity at room temperature with (a) mean grain size and (b) density of the 0.5Ga-LLZO SPS and SPS + CS pellets.

of the total ionic conductivity. Samples with a large ratio of grain/grain-boundaries are expected to have high values of total ionic conductivity.

Meanwhile, SPS + CS950 pellets displayed an ionic conductivity  $\sigma_b$  enhancement from  $1.61 \times 10^{-5}$  S/cm to  $2.16 \times 10^{-5}$  S/cm;  $\sigma_{gb}$  decrease from  $3.07 \times 10^{-6}$  S/cm to  $2.21 \times 10^{-6}$  S/cm which was potentially due to the enhanced re-distribution of gallium atoms at the grain boundaries after extended sintering times leading to higher resistance in the interfacial regions.

An obvious trend of an increase in the ionic conductivity with increased mean grain size and density are shown in Fig. 10 (a) and (b), respectively. From the perspective of grain size, a larger mean grain size indicates there are less interfacial areas in the pellets, and the contribution from grain boundaries become less than the bulk material. When density is taken into consideration, higher density provides more pathways for lithium ions transport across the material and the total ionic conductivity increases when more pathways are provided.

#### 4. Conclusion

Targeted compositions of LLZO have been synthesized via both a SG route and a solid state reaction route. The powders of Ga-doped LLZO are synthesized via the SG process results in smaller mean particle sizes ( $0.70 \pm 0.22 \mu\text{m}$ ) than those synthesized via SSR process ( $2.47 \pm 0.70 \mu\text{m}$ ). Smaller powder particle size means more interfacial surface area in the powders, which results in the larger grains and a more uniform grains distribution in the sintered pellets. The pellets were then sintered by both a spark plasma sintering process and a conventional sintering method. For SPS pellets, higher densification with smaller grain size was obtained, when it is compared with those fabricated by a conventional sintering process.

Many aspects such as crystalline phase, grain size, grain and grain boundaries characteristics, and sample density determine ionic conductivity. Due to the limited grain coarsening introduced via spark plasma sintering, the ionic conductivity of 0.5Ga-LLZO pellet fabricated by SPS was lower than those sintered by CS process. Controlled annealing studies resulting in grain growth of SPS samples indicated the total ionic conductivities were still reduced when multiple effects were taken into consideration. Sample sintered at  $1100^\circ\text{C}$  for 5 h directly from sol-gel powers displayed a larger grain size due to the higher activation energy of the powers, as compared with the samples that were initially SPS sintered before grain coarsening. The present work shows the process of grain coarsening for LLZO, providing information on the structure/property relations related to ionic conductivity including phase composition, grain size, and density.

#### Acknowledgement

We gratefully acknowledge support from the Department Materials Science and Engineering and the Electron Microscopy Laboratory at the Clemson University.

#### References

- [1] O. Crowther, A.C. West, Effect of electrolyte composition on lithium dendrite growth, *J. Electrochem. Soc.* 155 (2008) A806–A811.
- [2] J. Awaka, N. Kijima, H. Hayakawa, J. Akimoto, Synthesis and structure analysis of tetragonal  $\text{Li}_7\text{La}_3\text{Zr}_2\text{O}_{12}$  with the garnet-related type structure, *J. Solid State Chem.* 182 (2009) 2046–2052.
- [3] J.B. Goodenough, Rechargeable batteries: challenges old and new, *J. Solid State Electrochem.* 16 (2012) 2019–2029.
- [4] V. Thangadurai, H. Kaack, W.J.F. Weppner, Novel fast lithium ion conduction in garnet-type  $\text{Li}_5\text{La}_3\text{M}_2\text{O}_{12}$  (M = Nb, Ta), *J. Am. Ceram. Soc.* 86 (2003) 437–440.
- [5] V. Thangadurai, W. Weppner, Investigations on electrical conductivity and chemical compatibility between fast lithium ion conducting garnet-like  $\text{Li}_6\text{BaLa}_2\text{Ta}_2\text{O}_{12}$  and lithium battery cathodes, *J. Power Sources* 142 (2005) 339–344.
- [6] R. Murugan, V. Thangadurai, W. Weppner, Fast lithium ion conduction in garnet-type  $\text{Li}(7)\text{La}(3)\text{Zr}(2)\text{O}(12)$ , *Angew. Chem.* 46 (2007) 7778–7781.
- [7] L. Cheng, J.S. Park, H. Hou, V. Zorba, G. Chen, T. Richardson, J. Cabana, R. Russo, M. Doeff, Effect of microstructure and surface impurity segregation on the electrical and electrochemical properties of dense Al-substituted  $\text{Li}_7\text{La}_3\text{Zr}_2\text{O}_{12}$ , *J. Mater. Chem. A* 2 (2014) 172–181.
- [8] M.A. Huang, T. Liu, Y.F. Deng, H.X. Geng, Y. Shen, Y.H. Lin, C.W. Nan, Effect of sintering temperature on structure and ionic conductivity of  $\text{Li}-7(-)\text{xLa}_3\text{Zr}_2\text{O}_{12}-0.5\text{x}$  (x=0.5 similar to 0.7) ceramics, *Solid State Ionics* 204 (2011) 41–45.
- [9] J. Awaka, A. Takashima, K. Kataoka, N. Kijima, Y. Idemoto, J. Akimoto, Crystal structure of fast lithium-ion-conducting cubic  $\text{Li}_7\text{La}_3\text{Zr}_2\text{O}_{12}$ , *Chem. Lett.* 40 (2011) 60–62.
- [10] Y. Jin, P.J. McGinn, Al-doped  $\text{Li}_7\text{La}_3\text{Zr}_2\text{O}_{12}$  synthesized by a polymerized complex method, *J. Power Sources* 196 (2011) 8683–8687.
- [11] J.L. Allen, J. Wolfenstine, E. Rangasamy, J. Sakamoto, Effect of substitution (Ta, Al, Ga) on the conductivity of  $\text{Li}_7\text{La}_3\text{Zr}_2\text{O}_{12}$ , *J. Power Sources* 206 (2012) 315–319.
- [12] J. Wolfenstine, J. Sakamoto, J.L. Allen, Electron microscopy characterization of hot-pressed Al substituted  $\text{Li}_7\text{La}_3\text{Zr}_2\text{O}_{12}$ , *J. Mater. Sci.* 47 (2012) 4428–4431.
- [13] R.-J. Chen, M. Huang, W.-Z. Huang, Y. Shen, Y.-H. Lin, C.-W. Nan, Effect of calcining and Al doping on structure and conductivity of  $\text{Li}_7\text{La}_3\text{Zr}_2\text{O}_{12}$ , *Solid State Ionics* 265 (2014) 7–12.
- [14] F. Langer, J. Glenneberg, I. Bardenhagen, R. Kun, Synthesis of single phase cubic Al-substituted  $\text{Li}_7\text{La}_3\text{Zr}_2\text{O}_{12}$  by solid state lithiation of mixed hydroxides, *J. Alloys Compd.* 645 (2015) 64–69.
- [15] S. Kumazaki, Y. Iriyama, K.-H. Kim, R. Murugan, K. Tanabe, K. Yamamoto, T. Hirayama, Z. Ogumi, High lithium ion conductive  $\text{Li}_7\text{La}_3\text{Zr}_2\text{O}_{12}$  by inclusion of both Al and Si, *Electrochem. Commun.* 13 (2011) 509–512.
- [16] J. Wolfenstine, J. Ratchford, E. Rangasamy, J. Sakamoto, J.L. Allen, Synthesis and high Li-ion conductivity of Ga-stabilized cubic  $\text{Li}_7\text{La}_3\text{Zr}_2\text{O}_{12}$ , *Mater. Chem. Phys.* 134 (2012) 571–575.
- [17] H. El Shinawi, J. Janek, Stabilization of cubic lithium-stuffed garnets of the type “ $\text{Li}_7\text{La}_3\text{Zr}_2\text{O}_{12}$ ” by addition of gallium, *J. Power Sources* 225 (2013) 13–19.
- [18] T. Thompson, J. Wolfenstine, J.L. Allen, M. Johannes, A. Huq, I.N. David, J. Sakamoto, Tetragonal vs. cubic phase stability in Al – free Ta doped  $\text{Li}_7\text{La}_3\text{Zr}_2\text{O}_{12}$ (LLZO), *J. Mater. Chem. A* 2 (2014) 13431.
- [19] C. Liu, K. Rui, C. Shen, M.E. Badding, G. Zhang, Z. Wen, Reversible ion exchange and structural stability of garnet-type Nb-doped  $\text{Li}_7\text{La}_3\text{Zr}_2\text{O}_{12}$  in water for applications in lithium batteries, *J. Power Sources* 282 (2015) 286–293.
- [20] Y. Li, Z. Wang, Y. Cao, F. Du, C. Chen, Z. Cui, X. Guo, W-doped  $\text{Li}_7\text{La}_3\text{Zr}_2\text{O}_{12}$  ceramic electrolytes for solid state Li-ion batteries, *Electrochim. Acta* 180 (2015) 37–42.
- [21] S.W. Wang, Y.F. Liu, J. He, F.L. Chen, K.S. Brinkman, Spark-plasma-sintered barium zirconate based proton conductors for solid oxide fuel cell and hydrogen separation applications, *Int. J. Hydrogen Energy* 40 (2015) 5707–5714.
- [22] K. Brinkman, Y. Wang, M. Cantoni, D. Su, N. Setter, P.K. Petrov, Processing and properties of ferroelectric relaxor lead scandium tantalate  $\text{Pb}(\text{Sc}_{1/2}\text{Ta}_{1/2})\text{O}-3$  thin films, *J. Mater. Res.* 22 (2007) 217–232.
- [23] M. Kotobuki, H. Munakata, K. Kanamura, Y. Sato, T. Yoshida, Compatibility of  $\text{Li}[\text{sub } 7]\text{La}[\text{sub } 3]\text{Zr}[\text{sub } 2]\text{O}[\text{sub } 12]$  solid electrolyte to all-solid-state battery using Li metal anode, *J. Electrochem. Soc.* 157 (2010) A1076.
- [24] G. Larraz, A. Orera, M.L. Sanjuán, Cubic phases of garnet-type  $\text{Li}_7\text{La}_3\text{Zr}_2\text{O}_{12}$ : the role of hydration, *J. Mater. Chem. A* 1 (2013) 11419.
- [25] C. Bernuy-Lopez, W. Manalastas, J.M. Lopez del Amo, A. Aguadero, F. Aguesse, J.A. Kilner, Atmosphere controlled processing of Ga-Substituted garnets for high Li-Ion conductivity ceramics, *Chem. Mater.* 26 (2014) 3610–3617.
- [26] Y. Zhang, F. Chen, R. Tu, Q. Shen, L. Zhang, Field assisted sintering of dense Al-substituted cubic phase  $\text{Li}_7\text{La}_3\text{Zr}_2\text{O}_{12}$  solid electrolytes, *J. Power Sources* 268 (2014) 960–964.
- [27] I.N. David, T. Thompson, J. Wolfenstine, J.L. Allen, J. Sakamoto, B. Vijay, Microstructure and Li-Ion conductivity of hot-pressed cubic  $\text{Li}_7\text{La}_3\text{Zr}_2\text{O}_{12}$ , *J. Am. Ceram. Soc.* 98 (2015) 1209–1214.
- [28] N. Janani, S. Ramakumar, S. Kannan, R. Murugan, B. Dunn, Optimization of lithium content and sintering aid for maximized Li+Conductivity and density in Ta-Doped  $\text{Li}_7\text{La}_3\text{Zr}_2\text{O}_{12}$ , *J. Am. Ceram. Soc.* 98 (2015) 2039–2046.
- [29] H. Katsui, T. Goto, Preparation of cubic and tetragonal  $\text{Li}_7\text{La}_3\text{Zr}_2\text{O}_{12}$  film by metal organic chemical vapor deposition, *Thin Solid Films* 584 (2015) 130–134.
- [30] S. Mukhopadhyay, T. Thompson, J. Sakamoto, A. Huq, J. Wolfenstine, J.L. Allen, N. Bernstein, D.A. Stewart, M.D. Johannes, Structure and stoichiometry in supervalent doped  $\text{Li}_7\text{La}_3\text{Zr}_2\text{O}_{12}$ , *Chem. Mater.* 27 (2015) 3658–3665.
- [31] X. Tong, V. Thangadurai, E.D. Wachsman, Highly conductive Li garnets by a multielement doping strategy, *Inorg. Chem.* 54 (2015) 3600–3607.
- [32] C.-L. Tsai, E. Dashjav, E.-M. Hammer, M. Finsterbusch, F. Tietz, S. Uhlenbruck, H.P. Buchkremer, High conductivity of mixed phase Al-substituted  $\text{Li}_7\text{La}_3\text{Zr}_2\text{O}_{12}$ , *J. Electroceram.* 35 (2015) 25–32.
- [33] Y. Zhang, J. Cai, F. Chen, R. Tu, Q. Shen, X. Zhang, L. Zhang, Preparation of cubic  $\text{Li}_7\text{La}_3\text{Zr}_2\text{O}_{12}$  solid electrolyte using a nano-sized core-shell structured precursor, *J. Alloys Compd.* 644 (2015) 793–798.

- [34] M. Botros, R. Djenadic, O. Clemens, M. Möller, H. Hahn, Field assisted sintering of fine-grained  $\text{Li}_7-3x\text{La}_3\text{Zr}_2\text{Al}_x\text{O}_{12}$  solid electrolyte and the influence of the microstructure on the electrochemical performance, *J. Power Sources* 309 (2016) 108–115.
- [35] H.X. Geng, C. Kai, Y. Di, M. Ao, H. Mian, Y.H. Lin, N. Cewen, Formation mechanism of garnet-like  $\text{Li}_7\text{La}_3\text{Zr}_2\text{O}_{12}$  powder prepared by solid state reaction, *Rare Metal. Mat. Eng.* 45 (2016) 612–616.
- [36] Z. Hu, H. Liu, H. Ruan, R. Hu, Y. Su, L. Zhang, High Li-ion Conductivity of Al-doped  $\text{Li}_7\text{La}_3\text{Zr}_2\text{O}_{12}$  Synthesized by Solid-state Reaction, *Ceramics International*, 2016.
- [37] H. Jena, K.V.G. Kutty, T.R.N. Kutty, Studies on the ionic transport and structural investigations of  $\text{La}_{0.5}\text{Li}_{0.5}\text{TiO}_3$  perovskite synthesized by wet chemical methods and the effect of Ce, Zr substitution at Ti site, *J. Mater. Sci.* 40 (2005) 4737–4748.
- [38] L. Robben, E. Merzlyakova, P. Heitjans, T.M. Gesing, Symmetry reduction due to gallium substitution in the garnet  $\text{Li}_{6.43}(2)\text{Ga}_{0.52}(3)\text{La}_{2.67}(4)\text{Zr}_2\text{O}_{12}$ , *Acta crystallographica. Section E, Crystallogr. Commun.* 72 (2016) 287–289.
- [39] N. Rosenkowitz, J. Schuhmacher, M. Bockmeyer, J. Deubener, Nitrogen-free sol–gel synthesis of Al-substituted cubic garnet  $\text{Li}_7\text{La}_3\text{Zr}_2\text{O}_{12}$  (LLZO), *J. Power Sources* 278 (2015) 104–108.
- [40] Z. Cao, X. Cao, X. Liu, W. He, Y. Gao, J. Liu, J. Zeng, Effect of Sb-Ba codoping on the ionic conductivity of  $\text{Li}_7\text{La}_3\text{Zr}_2\text{O}_{12}$  ceramic, *Ceram. Int.* 41 (2015) 6232–6236.
- [41] A. Logeat, T. Koehler, U. Eisele, B. Stiaszny, A. Harzer, M. Tovar, A. Senyshyn, H. Ehrenberg, B. Kozinsky, From order to disorder: the structure of lithium-conducting garnets  $\text{Li}_7-x\text{La}_3\text{TaxZr}_2-x\text{O}_{12}$  ( $x=0-2$ ), *Solid State Ionics* 206 (2012) 33–38.
- [42] C.A. Geiger, E. Alekseev, B. Lazic, M. Fisch, T. Armbruster, R. Langner, M. Fechtelkord, N. Kim, T. Pettke, W. Weppner, Crystal chemistry and stability of "Li $_7\text{La}_3\text{Zr}_2\text{O}_{12}$ " garnet: a fast lithium-ion conductor, *Inorg. Chem.* 50 (2011) 1089–1097.
- [43] T.J. Collins, ImageJ for microscopy, *Biotechniques* 43 (2007), 25–+.
- [44] T. Norby, Proton conduction in solids: bulk and interfaces, *Mrs Bull.* 34 (2009) 923–928.